ARTICLE

In Situ Microscopic Studies on the Interaction of Multi-Principal Element Nanoparticles and Bacteria

Abhijit H. Phakatkar, Vitaliy Yurkiv, Pankaj Ghildiyal, Yujie Wang, Azadeh Amiri, Lioudmila V. Sorokina, Michael R. Zachariah, Tolou Shokuhfar,* and Reza Shahbazian-Yassar*

Cite This: https://doi.org/10.1021/acsnano.2c12799

Read Online

| ACCESS | | Metrics & More | | Article Recommendations | | Supporting Information |

ABSTRACT: Multi-principal element nanoparticles are an emerging class of materials with potential applications in medicine and biology. However, it is not known how such nanoparticles interact with bacteria at nanoscale. In the present work, we evaluated the interaction of multi-principal elemental alloy (FeNiCu) nanoparticles with *Escherichia coli* (*E. coli*) bacteria using the *in situ* graphene liquid cell (GLC) scanning transmission electron microscopy (STEM) approach. The imaging revealed the details of bacteria wall damage in the vicinity of nanoparticles. The chemical mappings of S, P, O, N, C, and Cl elements confirmed the cytoplasmic leakage of the bacteria. Our results show that there is selective release of metal ions from the nanoparticles. The release of copper ions was much higher than that for nickel while the iron release was the lowest. In addition, the binding affinity of bacterial cell membrane protein functional groups with Cu, Ni, and Fe cations is found to be the driving force behind the selective metal cations' release from the multi-principal element nanoparticles. The protein functional groups driven dissolution of multielement nanoparticles was evaluated using the density functional theory (DFT) computational method, which confirmed that the energy required to remove Cu atoms from the nanoparticle surface was the least in comparison with those for Ni and Fe atoms. The DFT results support the experimental data, indicating that the energy to dissolve metal atoms exposed to oxidation and/or the to presence of oxygen atoms at the surface of the nanoparticle catalyzes metal removal from the multielement nanoparticle. The study shows the potential of compositional design of multi-principal element nanoparticles for the controlled release of metal ions to develop antibacterial strategies. In addition, GLC-STEM is a promising approach for understanding the nanoscale interaction of metallic nanoparticles with biological structures.

KEYWORDS: *scanning transmission electron microscopy, graphene liquid cell, bacteria, nanoparticles, antibacterial, multielement*
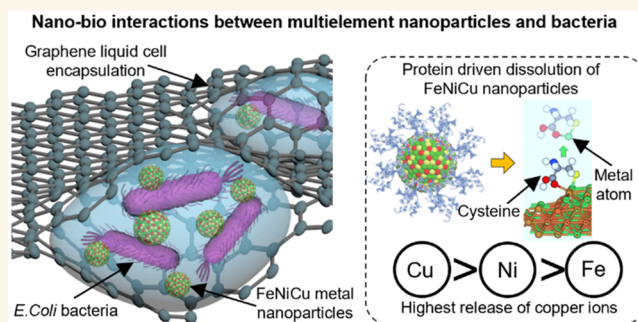
INTRODUCTION

Antimicrobial resistance (AMR) in bacteria is recently recognized as a "hidden pandemic" at the global healthcare platform.[1] Inorganic metal and metal oxide nanoparticles have shown promising potential addressing the challenge of continuously emerging AMR in bacteria.[2,3] Metal and metal oxide nanoparticles can exhibit bactericidal efficacy via various mechanisms, mainly as generation of reactive oxygen species (ROS), metal cations release, physical damage to the cellular membrane, and chemical binding with functional membrane proteins.[4] Released metal ions from the metallic and metal oxide nanoparticles can disintegrate DNA helical strands and can also inactivate thiol (-SH) groups in metabolic proteins.[5] Despite the proven antibacterial efficacy of metal and metal

oxide nanoparticles, there are reports of the developed AMR in bacteria due to the repetitive use of monometallic nanoparticles.[6−9] As an alternative to monometallic nanoparticles, recently research efforts were made with bimetallic nanoparticles to achieve higher antibacterial efficacy.[10] Benetti et al.[11] showed that the tailored multielement Ag−Cu−Mg nanoparticles are capable of killing a wide spectrum of
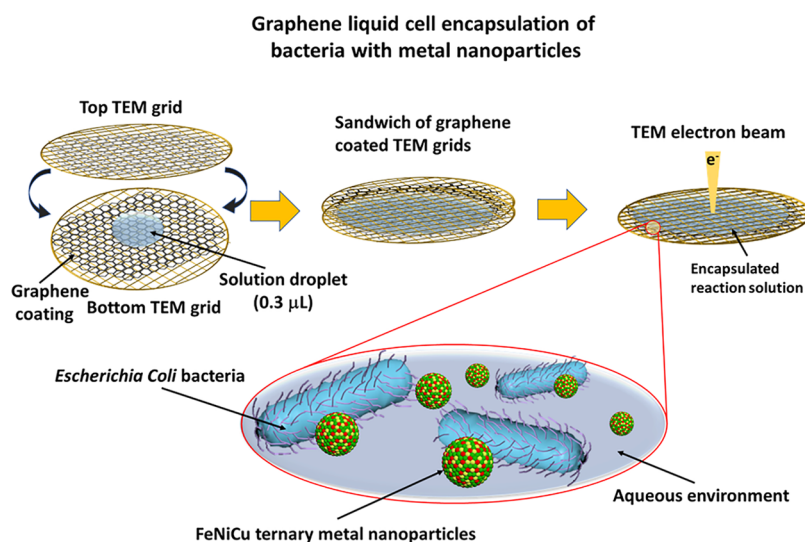
Figure 1. Schematic representation of graphene liquid cell-based approach for studying the interaction of multi-principal element nanoparticles with bacteria. Representative schematic highlighting the encapsulation of bacteria and metal nanoparticles using graphene coated TEM-gold grids.

Gram-negative and Gram-positive bacteria as compared with the respective unary metal nanoparticles. Zhang et al.[12] showed that ternary alloyed nanocomposites $(Ag/TiO_2/NaYF_4@Yb:Tm)$ are capable of generating ROS at both ambient light and solar simulator irradiation, exhibiting superior biocidal activity as compared with binary (Ag/TiO_2) nanocomposites. Alloying of multiple elements in a single nanoparticle led to a paradigm shift in designing of antibacterial nanoparticles capable of treating multidrug resistant bacteria.[13,14]

Developing strategies to investigate the nanoscale antibacterial mechanisms of metal and metal oxide nanoparticles is of utmost importance. Among the various available means for studying nanoscale antibacterial activities of nanomaterials, transmission electron microscopy (TEM) has emerged as a promising technique due to combined imaging and spectroscopic capabilities at sub-nanometer scale. Conventionally, cryo-TEM and resin-embedded ultramicrotome TEM ultrathin cross sections are utilized for studying localized nanoscale interactions of nanoparticles with bacteria.[15,16] These conventional TEM approaches have provided fundamental insights of nanoparticles' internalization (endocytosis) mechanisms in bacteria based on the physical and chemical characteristics of nanoparticles.[17,18] There exist the limitations with speculations made from these conventional TEM approaches, as only aliquots from the temporal studies could be considered. The resin-embedded ultramicrotome TEM approach possesses advantages with achieving higher signal-to-noise ratio and being radiation resistant, while there exist limitations with possible intrusion of structural artifacts due to specimen dehydration and negative-staining.[19] The cryo-TEM approach has advantages for preserving the native structure of a biological specimen, as no staining or dehydration/fixation is required, while as a shortcoming along with radiation sensitivity the imaging contrast gets affected due to low signal-to noise ratio and freezing artifacts.[19] Moreover, both the approaches require time-consuming and complicated TEM specimen preparation steps.

To address the limitations of the conventional TEM approaches, *in situ* TEM techniques can play an important role by providing insights on the time-lapsed nanoscale nano-

bio interactions. Using silicon nitride membranes for the *in situ* liquid scanning transmission electron microscopy (STEM) technique, Kennedy et al.[20] observed the interaction between *Escherichia coli (E. coli)* bacteria with P1 bacteriophage viruses. Recently, Kuo et al.[21] observed the real time interaction between glutathione-conjugated gold nanoclusters with *Acetobacter aceti* bacteria. As an alternative to silicon nitride membranes, the graphene liquid cell (GLC) is shown to be effective to study biological processes.[22−24] GLCs are capable of acquiring atomic resolution imaging with higher signal-to-noise ratio and can mitigate the charging effects and radiolysis damages.[25] In the past decade, few studies have shown potential to encapsulate bacteria in GLC microreactors.[26,27] The properties of graphene attributed to electrical conductivity, high thermal conductivity, high yield strength, electron transparency, flexibility, and impermeability make them suitable for TEM studies.[27] Graphene monolayers contributing to the *in situ* liquid TEM system can keep the beam sensitive sample hydrated during dynamic events' observations at nanoscale.[26,28] Moreover, the graphene can efficaciously scavenge reactive radical species, avoiding the radiolysis damage to beam sensitive materials.[29]

In the present work, we conducted a systematic study on the interaction of unary and multi-principal elemental nanoparticles with *E. coli* bacteria via the GLC-STEM approach. STEM-energy dispersive X-ray spectroscopy (EDS) results provide key insights on competitive metal cations' release from multi-principal element FeNiCu nanoparticles in the vicinity of *E. coli* bacteria. Additionally, the variations in the metal cations' release from unary Fe, Ni, and Cu nanoparticles were studied to understand the metal ions' release mechanism of action from ternary FeNiCu metal nanoparticles. STEM-EDS results also provide insights on morphological changes appearing in the bacterial cell integrity upon interaction with metal nanoparticles by tracing C, O, N, S, P, and Cl diagnostic elements from cellular components. The competitive release between copper, nickel and iron metal cations provides insights on the protein-driven metal nanoparticles' dissolution mechanism.
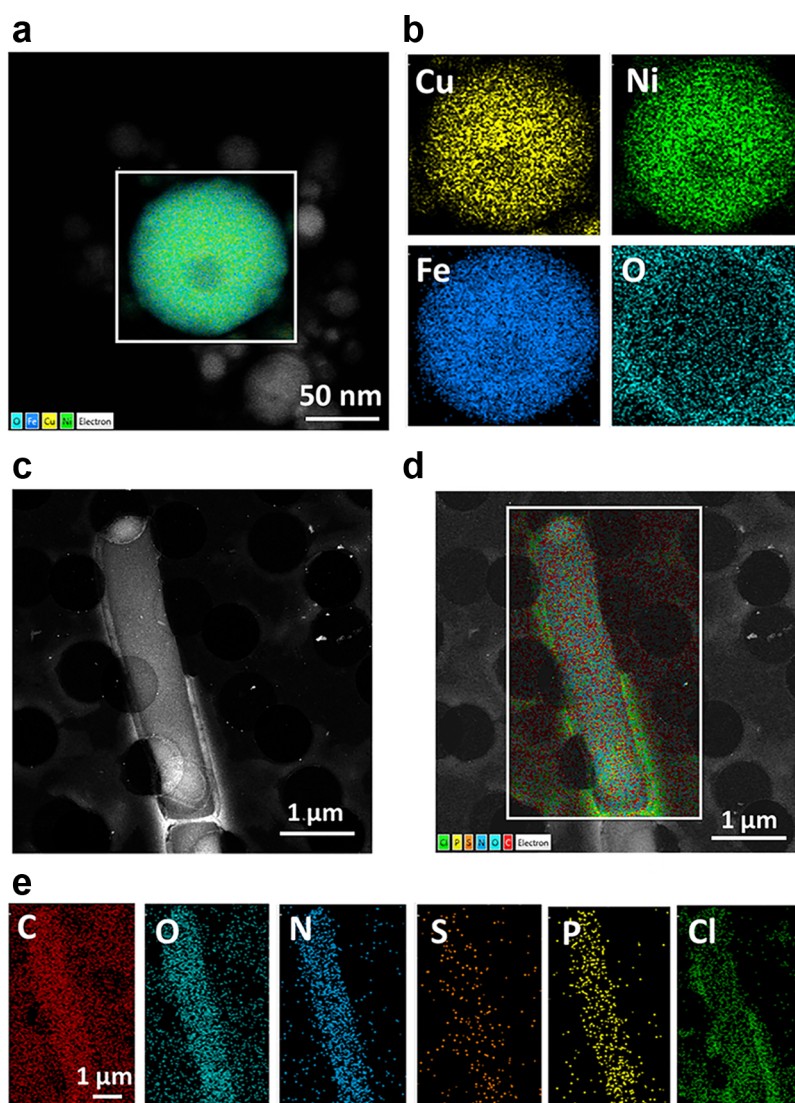
Figure 2. STEM-EDS analysis of the control specimens: (a−b) a FeNiCu ternary metal nanoparticle upon encapsulation in a GLC without bacteria; and (c−e) as-cultured *E. coli* bacteria without exposure to ternary metal nanoparticles. (a) EDS elemental analysis of a ternary metal nanoparticle encapsulated in the graphene liquid cell nanoreactors in the absence of bacteria indicating the mixed elemental mapping. (b) Corresponding STEM-EDS elemental maps of Fe, Ni, Cu, and O elements confirming the homogeneous presence of metal cations. (c) STEM-HAADF micrograph of control *E. coli* bacterium. (d) Corresponding EDS elemental mapping of *E. coli* bacterium confirming the presence of C, O, N, S, P, and Cl elements. (e) STEM-EDS elemental analysis of individual C, O, N, S, P, and Cl characteristic diagnostic elements indicating their distribution across the bacterium.

RESULTS AND DISCUSSION

In the present study, the elemental design for the ternary alloy nanoparticles was based on the potential antibacterial activity of the elements. Copper is well-known for its "contact killing" mechanisms, which include bacterial cell membrane damage, DNA degradation, reactive oxygen species (ROS) generation, and binding and denaturing of cell membrane proteins.[30] Iron exhibits antibacterial activity predominantly via Fenton reactions, ROS generation, and inactivation of membrane proteins by binding with carboxyl (-COOH), amino (-NH), and mecapto (-SH) functional groups.[31] Nickel contributes to antibacterial activity by reacting with phosphorus and sulfur containing cellular compounds and by damaging the bacterial cell membrane permeability.[32] As such, FeNiCu ternary metal nanoparticles (average diameter ∼90 nm) were synthesized using the aerosol spray pyrolysis method and the details were reported in our earlier work.[33] For future studies one should take into account the effect of size variation of nanoparticles, valence of elements, and structure of nanoparticles.

The schematic representation of the *in situ* GLC STEM approach for studying metallic nanoparticles and bacteria is shown in Figure 1. The solution encapsulated between the graphene coated TEM grids contains *E. coli* bacteria and multi-principal element nanoparticles. Figures S1a and S1b show the STEM-HAADF micrographs and STEM-EDS elemental characterization of FeNiCu ternary metal nanoparticles, respectively, before encapsulating in a GLC. STEM-EDS results show that the evaluated elemental composition of FeNiCu ternary metal nanoparticles was Fe (34.24 at%), Ni (33.02 at%), and Cu (32.74 at%), suggesting near equimolar concentration. The corresponding EDS spectrum clearly shows distinct $K_{\alpha 1}$ characteristic elemental edges of Fe, Ni, and Cu elements at 6.404 eV, 7.478 keV, and 8.048 keV, respectively. Similarly, distinct $K_{\beta 1}$ characteristic elemental edges in the
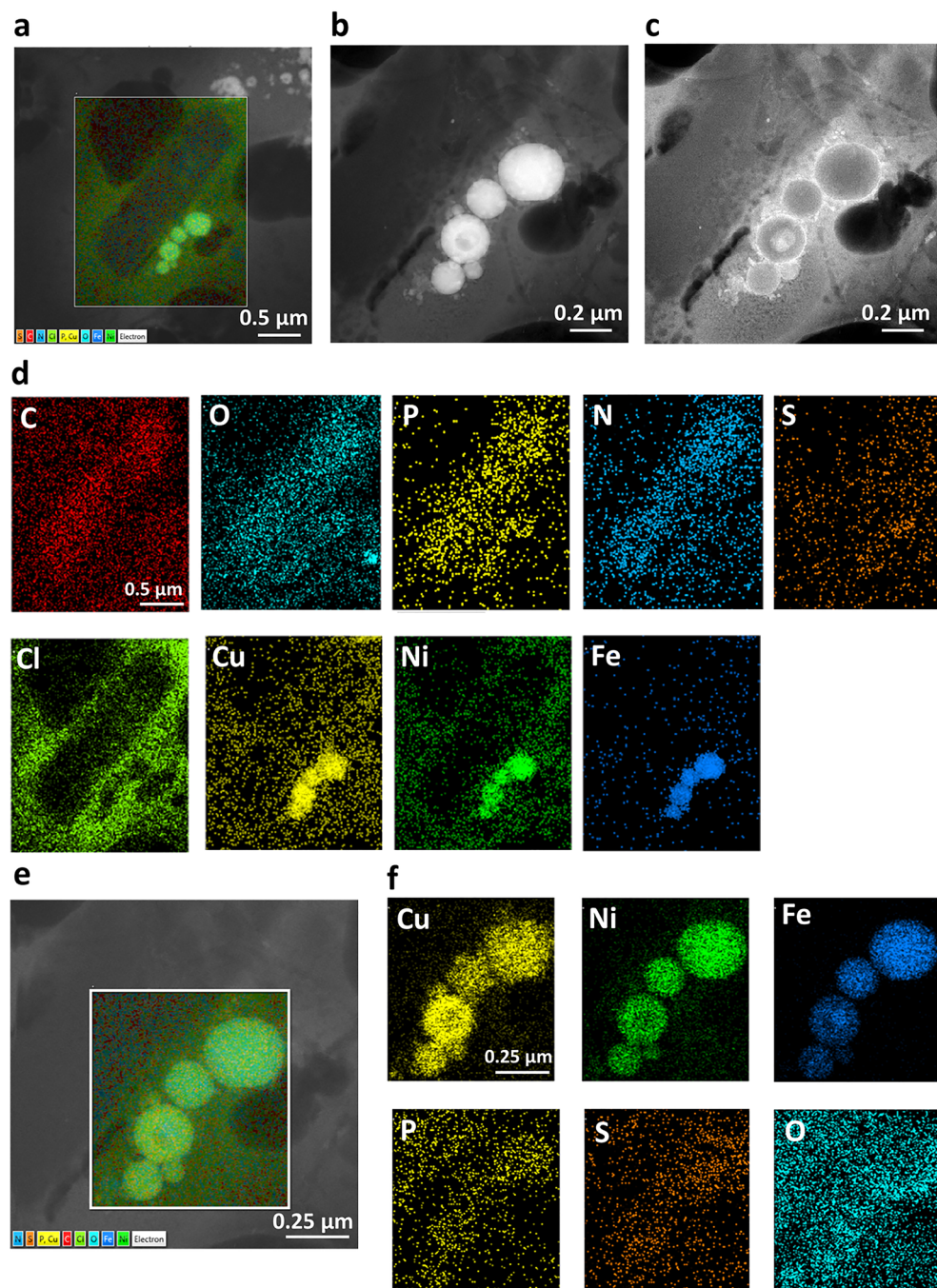
Figure 3. STEM elemental analysis of *E. coli* bacterium in the presence of FeNiCu ternary metal nanoparticles acquired in a GLC. (a) EDS elemental mapping of *E. coli* bacterium in contact with ternary metal nanoparticles. (b) STEM-HAADF micrograph of a magnified region of ternary metal nanoparticles interacting with the *E. coli* bacterium cell membrane highlighting the brighter contrast of Fe, Ni, and Cu transition elements. (c) STEM-LAADF micrograph of a magnified region of ternary nanoparticles interacting with the *E. coli* bacterium cell membrane, highlighting the brighter contrast of bacterium cytoplasmic contents. (d) STEM-EDS elemental mapping of *E. coli* bacterium in contact with ternary metal nanoparticles confirming the Fe, Ni, and Cu metal cations release inside the bacterium and the leakage of cellular cytoplasmic components with diagnostically characteristic C, O, P, N, S, and Cl elements. (e) STEM-EDS elemental mapping from the same magnified region highlighting the changes in the metal nanoparticles. (f) STEM-EDS elemental mapping of individual Cu, Ni, Fe, P, S, and O elements confirming the higher leaching of Cu cations from the nanoparticles in comparison with Ni and Fe elements.

EDS spectrum for Fe, Ni, and Cu elements can be observed at 7.058 keV, 8.265 keV, and 8.905 keV, respectively.

In the next step, chemical investigations were performed to understand any possible chemical change upon suspending nanoparticles in the ultrapure water aqueous environment in the absence of bacteria. Figure 2 shows the STEM characterization of FeNiCu nanoparticles while suspended in the aqueous environment in a GLC. Figure 2a shows STEM-EDS mixed elemental mapping of an FeNiCu ternary nanoparticle confirming the homogeneous composition of Fe, Ni, an Cu elements. The corresponding individual elemental mappings of Fe, Ni, Cu, and O elements are represented in Figure 2b. Oxygen elemental mapping confirms the slight surface oxidation of transition metals from FeNiCu ternary nano-
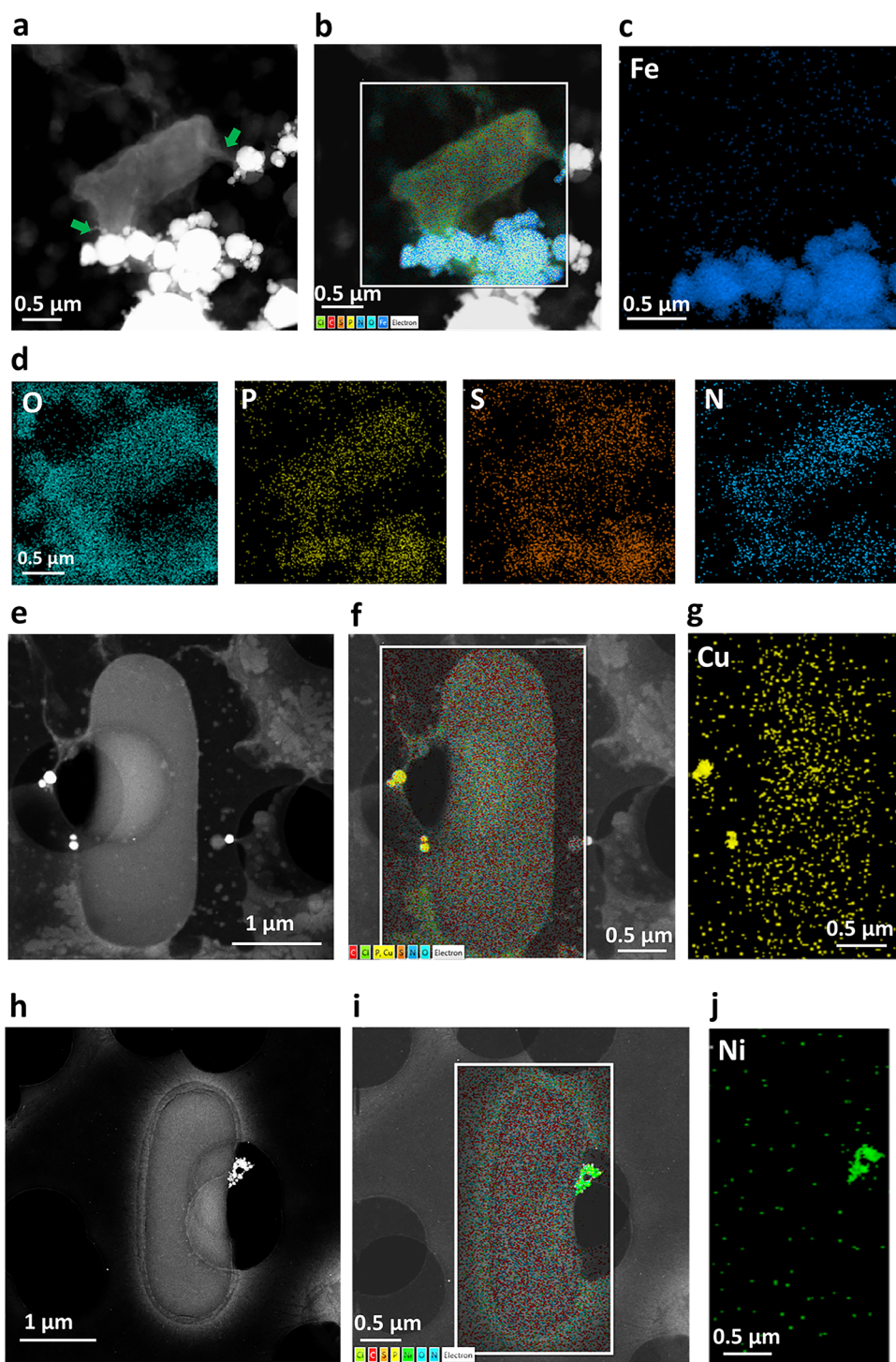
Figure 4. STEM elemental analysis of as cultured *E. coli* bacterium in the presence of unary Fe, unary Ni, and unary Cu metal nanoparticles. (a) STEM-HHADF micrograph of *E. coli* bacterium in the presence of unary Fe metal nanoparticles. Green arrows indicate the cytoplasmic leakage from the bacterium. (b) Corresponding EDS mapping of *E. coli* bacterium in the vicinity of unary Fe metal nanoparticles. (c) STEM-EDS elemental mapping of Fe confirming no significant release of Fe metal cations in the bacterium cytoplasm from the unary Fe nanoparticles. (d) STEM-EDS elemental mapping of O, P, S, and N diagnostically characteristic elements indicating the leakage of bacterium cytoplasmic components. (e) STEM-HAADF micrograph of *E. coli* bacterium in the vicinity of unary Cu nanoparticles. (f) STEM-EDS elemental mapping of *E. coli* bacterium in the vicinity of unary Cu metal nanoparticles confirming the presence of C, O, P, S, N, Cl, and Cu elements. (g) Corresponding STEM-EDS elemental mapping of *E. coli* bacterium confirming the significant release of Cu cations in the bacterium cytoplasm. (h) STEM-HAADF micrograph of *E. coli* bacterium in the vicinity of unary Ni metal nanoparticles. (i) Corresponding STEM-EDS elemental mapping of *E. coli* bacterium in the vicinity of unary nickel nanoparticles confirming the presence of C, O, P, S, N, Cl, and Ni elements. (j) Corresponding STEM-EDS elemental mapping of *E. coli* bacterium confirming no significant release of Ni cations from the unary Ni nanoparticles in the bacterium cytoplasm.

particles. The STEM-EDS elemental maps indicate no release of metal cations in the absence of bacteria.

Furthermore, STEM imaging and EDS analyses were performed on *E. coli* bacteria to characterize the chemical composition of bacteria in a GLC before exposure to nanoparticles. In an *in situ* liquid TEM system, the lethal electron dose (at 300 kV accelerating voltage) for bacterial cells was evaluated as 0.30 e$^-$/Å^2/frame using silicon nitride (Si$_3$N$_4$) membranes.[20] Graphene can further reduce the radiolysis damage for a biological specimen as compared with silicon nitride membranes.[25,26] In the present study, with the *in situ* GLC STEM approach, the maximum electron dose rate of 0.34 e$^-$/Å^2/s (at 200 kV accelerating voltage) was maintained, where no bacterial cell membrane damage was observed. Figures 2c–2e show the *in situ* GLC STEM-EDS elemental analysis of as-cultured control *E. coli* bacterium without treating with metal nanoparticles. Figure 2c shows the HAADF-STEM image of *E. coli* bacterium in the hydrated state. The corresponding STEM-EDS mixed elemental mapping is represented in Figure 2d. Figure 2e represents an individual elemental mapping of characteristic C, O, N, S, P, and Cl elements highlighting the components of the bacterial cytoplasm along with the cell membrane. Although the *E. coli* bacterium cellular structure is quite complex, the detection of these diagnostic ions can provide insights on the cellular structural integrity.[34] Phosphorus diagnostic ions are predominantly a part of deoxyribonucleic acid (DNA), phospholipids, and phosphorylated proteins in the bacterial cell.[5,35] Sulfur is present in the bacteria as building blocks of proteins mainly in cysteine and methionine amino acids.[35] Nitrogen is present as a major constituent in all amino acids in the bacterial cell.[36] Carbon is a major component of all organic cellular components in the cytoplasm and bacterial cell membrane.[36] Oxygen is present in proteins, carbohydrates, fatty acids, nucleic acids, and polyphosphates.[37] Chlorine is responsible for cellular homeostasis and plays an important role in osmotic balance in the bacterial cell.[35] As represented in Figure 2, STEM-EDS analysis of as-cultured control *E. coli* bacterium confirms the retained cellular structural integrity in the hydrated state upon encapsulation in a GLC. Additional locations of STEM-EDS analysis of as-cultured control *E. coli* bacteria are represented in Figure S2 in the Supporting Information.

Figure S3 shows the TEM and STEM micrographs of FeNiCu ternary metal nanoparticles in the vicinity of *E. coli* bacteria upon encapsulating in the aqueous environment in a GLC. Figure S3a represents the TEM micrographs of FeNiCu ternary metal nanoparticles in the vicinity of *E. coli* bacteria. The same region of interest was analyzed using STEM-HAADF and STEM-LAADF imaging modes as shown in Figures S3b and S3c, respectively. STEM-HAADF imaging mode achieves brighter imaging contrast for heavier elements, such as Fe, Ni, and Cu transition metals. As a result, the ternary metal nanoparticles appear brighter in the STEM-HAADF imaging mode as compared with *E. coli* bacteria as shown in Figure S3b. On the other hand, STEM-LAADF imaging mode achieved brighter contrast for lighter elements, such as C, N, O, P, and S elements composed within the bacterial cell components. In Figure S3c brighter contrast for bacterial cells and for organic corona around the nanoparticles can be observed, where FeNiCu ternary metal nanoparticles demonstrate lower contrast. The atomic number-based Z-

contrast imaging in the STEM mode can provide insights on the morphological changes that occurred in the bacterial cells.

Figure 3 represents the STEM-EDS analysis of *E. coli* bacteria in the presence of FeNiCu ternary metal nanoparticles in a GLC. Upon treating with FeNiCu ternary metal nanoparticles, it is evident that the *E. coli* bacteria lost their structural integrity (compared with Figures 2c–e). Figure 3a shows the STEM-EDS analysis of mixed elemental mapping of *E. coli* bacteria with membrane attached FeNiCu ternary metal nanoparticles. Figures 3b and c show STEM-HAADF and STEM-LAADF micrographs from the same region of interest. In Figure 3c brighter contrast around the ternary nanoparticles can be observed indicating the leakage of bacterial cytoplasmic components. In Figure 3d corresponding STEM-EDS elemental maps of C, O, P, N, S, Cl, Fe, Ni, and Cu individual elements are represented. The STEM-EDS analysis of diagnostic elements C, O, P, N, S, and Cl from *E. coli* bacteria confirms the localized leakage of bacterium cytoplasm and the lost cellular integrity upon interacting with bacteria. As observed in Figure 3c, the bacterium cytoplasmic corona formation around the nanoparticles can be confirmed with STEM-EDS elemental mapping of the elements. Moreover, the STEM-EDS elemental maps of Fe, Ni, and Cu provide insights on the multiple metal ions released from the FeNiCu ternary metal nanoparticles. The variation in the metal cations release from FeNiCu ternary metal nanoparticles can be observed qualitatively in Figure 3d. The release of copper cations from FeNiCu nanoparticles was significantly higher followed by nickel cations and then by iron cations. The released metal cations are observed inside the bacterium cytoplasm. Figure 3e shows the STEM-EDS mixed elemental mapping of the same region with a higher magnification to gain insights on the modifications occurring in FeNiCu ternary metal nanoparticles. Corresponding STEM-EDS elemental mappings of Fe, Ni, Cu, P, S, and O individual elements are represented in Figure 3f. STEM-EDS elemental maps of P, S, O confirm the localized leakage of bacterium cellular components around the ternary metal nanoparticles. While STEM-EDS elemental mapping of Cu, Ni, and Fe clearly show the higher outer diffusion of copper cations from the FeNiCu ternary nanoparticles in comparison to Fe and Ni. Nickel cations were observed to have lower outer diffusion in FeNiCu nanoparticles than those of copper cations. Iron cations were observed to have least release, predominantly maintaining the occupancy in the crystal lattice of FeNiCu nanoparticles. Additional locations of STEM-EDS analysis of interaction of *E. coli* bacteria with FeNiCu ternary metal nanoparticles are represented in Figure S4 in the Supporting Information.

To further investigate the competitive multi-principal element metal ions' release from the FeNiCu ternary metal nanoparticles, metal ions' release from the unary Fe, unary Ni, and unary Cu metal nanoparticles was studied to gain deeper insights. Figure 4 shows the STEM-EDS analysis of *E. coli* bacteria after treating with unary Fe, unary Ni, and unary Cu metal nanoparticles. Figure 4a represents the HAADF-STEM micrograph of *E. coli* bacterium upon treating with unary Fe metal nanoparticles. Green arrows indicate the localized leakage of bacterium cytoplasm in contact with unary Fe metal nanoparticles. The corresponding STEM-EDS mixed elemental mapping can be observed in Figure 4b. Figure 4c represented STEM-EDS elemental mapping of Fe, where almost no release of iron cations from nanoparticles was observed in the bacterium cytoplasm. These observations were
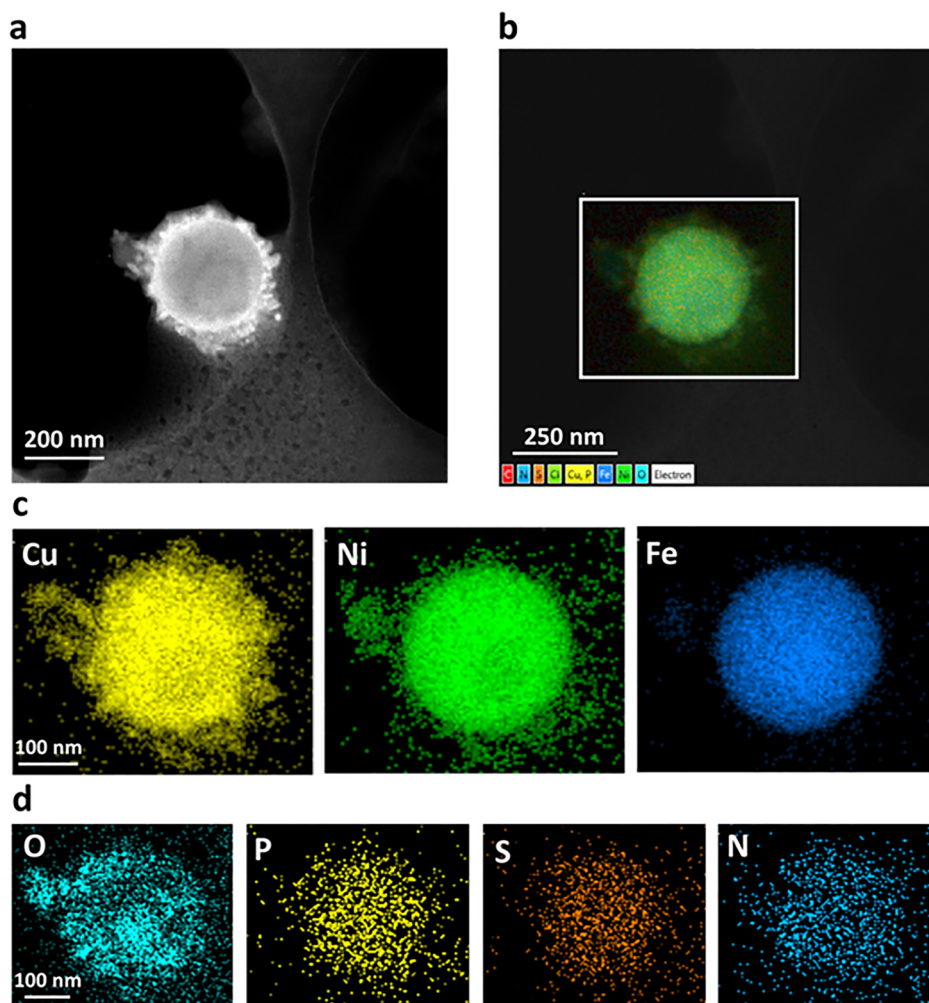
Figure 5. STEM elemental analysis of FeNiCu ternary metal nanoparticle upon interacting with *E. coli* bacteria. (a) STEM-LAADF micrograph of FeNiCu ternary metal nanoparticle highlighting the brighter contrast of the organic corona around a nanoparticle. (b) STEM-EDS elemental mapping of FeNiCu ternary metal nanoparticle along with the organic corona around a nanoparticle. (c) STEM-EDS elemental mapping of individual Cu, Ni, and Fe elements confirming the release of metal cations from the FeNiCu ternary metal nanoparticles. (d) STEM-EDS elemental mapping of diagnostic O, P, S, and N elements indicating bacterial cytoplasmic components contributing to the organic corona around a nanoparticle.

consistent with bacterium interaction with FeNiCu ternary metal nanoparticles. Figure 4d represents the STEM-EDS elemental mapping of *E. coli* bacterium, where O, P, S, and N diagnostic elements are observed. STEM-EDS elemental mapping of O, P, S, and N indicates the leakage of cytoplasmic components in the localized region of unary metal nanoparticles. Figure 4e shows the HAADF-STEM micrograph of *E. coli* bacterium in the presence of unary Cu metal nanoparticles. The corresponding STEM-EDS elemental mixed mapping is represented in Figure 4f, where C, O, P, Cl, S, N, and Cu elements are present. Figure 4g shows the STEM-EDS elemental mapping of Cu, where significantly released copper cations inside the bacterium cytoplasm are observed. Figure 4h represents the HAADF-STEM micrograph of *E. coli* bacterium in the presence of unary Ni metal nanoparticles. The corresponding STEM-EDS elemental mixed mapping is represented in Figure 4i, where C, O, P, Cl, S, N, and Ni elements are present. STEM-EDS elemental mapping of Ni is represented in Figure 4j, where almost no significant release of Ni cations inside bacterium was observed from unary Ni metal nanoparticles. The observation of significant release of copper

cations from unary Cu metal nanoparticles was in line with the highest copper ions release as observed from FeNiCu ternary metal nanoparticles as compared with iron and nickel metal cations. It is important to note that in FeNiCu ternary metal nanoparticles, the release of copper cations appears to be more favorable than the release of Ni metal cations in the vicinity of bacteria. This is supported by the data showing no detectable release of Ni from unary Ni metal nanoparticles when exposed to bacteria. Additional locations of STEM-EDS analysis of interaction of *E. coli* bacteria with unary-Fe, unary-Ni, and unary-Cu metal nanoparticles are represented in Figure S5 in the Supporting Information.

Higher release of copper cations from FeNiCu ternary metal nanoparticles was observed in the organic corona around a metal nanoparticle. FeNiCu ternary nanoparticles upon interacting with bacteria for 10 min were observed for any morphological changes. Figure 5 shows the STEM-EDS analysis of FeNiCu ternary metal nanoparticles surrounded by organic corona which formed upon interacting with *E. coli* bacteria. Figure 5a represents the LAADF-STEM micrograph of a FeNiCu ternary metal nanoparticle, where brighter
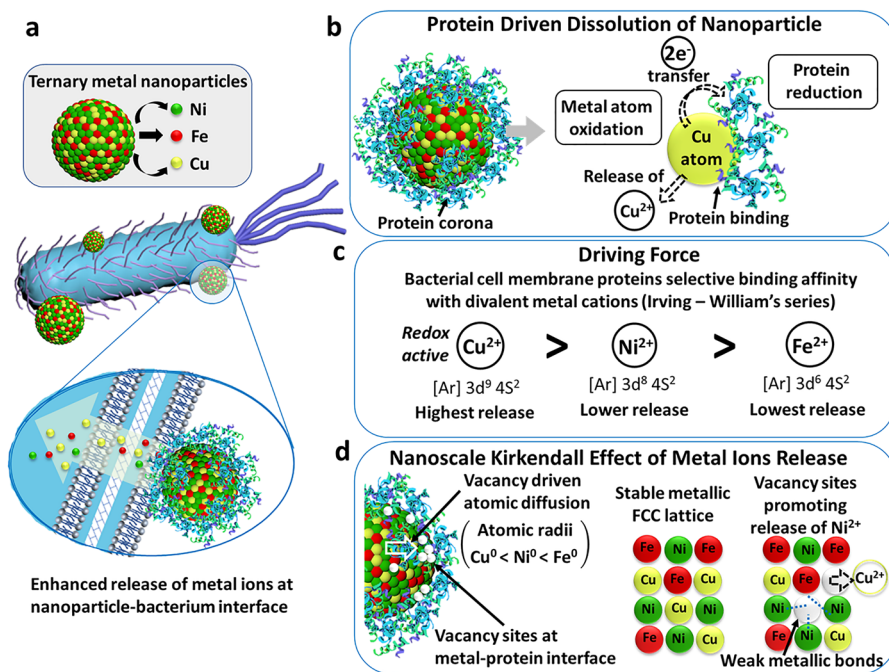
Figure 6. Proposed pathways of antibacterial metal ions' release from the ternary FeNiCu nanoparticles in the vicinity of the bacterial cell membrane. (a) Representative schematic of FeNiCu ternary metal nanoparticles attached with an *E. coli* bacterium cell membrane. (b) Schematic representation of protein driven oxidative dissolution of nanoparticles. (c) Representation of selective binding affinity variation of divalent Cu^{2+}, Ni^{2+}, and Fe^{2+} metal cations with bacterial cell membrane proteins. (d) Representative schematic of the nanoscale Kirkendall effect highlighting atomic vacancy driven metal ions' release.

contrast of the organic corona around a nanoparticle is evident. The corresponding STEM-EDS mixed elemental mapping of an FeNiCu ternary metal nanoparticle surrounded by an organic corona is shown in Figure 5b. Figure 5c shows STEM-EDS elemental mappings of Fe, Ni, and Cu individual elements. Similar to the release of multiple metal cations in the vicinity of bacteria, the release of copper cations was highest in the organic corona around a nanoparticle followed by nickel cations and then least by iron cations. The outward diffusion of copper cations followed by nickel cations can be clearly observed in the organic corona, while the iron cations seem to have the lowest outward diffusion from the FeNiCu ternary metal nanoparticle. Figure 5d shows the STEM-EDS elemental mappings of individual O, P, and N elements. These diagnostic elements are observed in *E. coli* bacterium cytoplasmic and cell membrane components. These STEM-EDS elemental maps of diagnostic ions suggest that the presence of bacterial cellular proteins resulted in the formation of an organic corona around a nanoparticle. Metal nanoparticles can form a protein corona upon contact with distinct biomolecules, attributed to their chemical composition, size, surface functionality, and charge.[38,39] It is interesting to note that in the absence of direct contact with bacteria, leaked cytoplasmic or cell membrane components from bacteria can trigger metal ions' release from FeNiCu ternary metal nanoparticles.

The release of multiple metal cations from FeNiCu ternary metal nanoparticles suggests that the functional groups present in the bacterial cell membrane or cytoplasmic components can trigger the release of metal cations.[40] By taking into consideration these various observations, we propose that the protein driven oxidative dissolution mechanism could be playing a vital role in different metal cations' release from multi-principal element nanoparticles. Figure 6 shows the

schematic representation of various pathways where metal ions' release antibacterial mechanisms of action can be explained. In the present study, a consistent +2 valence state of Fe^{2+}, Ni^{2+}, and Cu^{2+} metal cations is assumed considering the limitations and challenges associated with probing the valence states of metal cations in bacterium cytoplasm using X-ray photoelectron spectroscopy (XPS) and STEM-electron energy loss spectroscopy (EELS) techniques.

Figure 6a represents a schematic of an organic corona formed around a FeNiCu ternary metal nanoparticle upon direct contact with the bacterial cell membrane. The *in situ* GLC STEM-EDS results of P, S, N, and O diagnostic elements confirm the formation of an organic corona around metal nanoparticles at the nano-bio interface. Cell membrane proteins can get adsorbed on metal nanoparticles forming an organic corona around a nanoparticle.[41] Upon formation of a protein corona around a metal nanoparticle, oxidative dissolution of metal nanoparticles can take place. The organothiol (R-SH) functional groups present in cysteine and methionine proteins can promote progressive degradation of silver nanoparticles.[42] Fukushima et al.[43] confirmed that electron transfer can take place between proteins bound with metal oxides. Martinolich et al.[44] have shown the Cu-metalloproteins driven oxidative dissolution of silver nano-particles. Recently, Ali et al.[45] showed the protein driven dissolution of silica nanoparticles via charge transfer between a positively charged amino acid in the protein with the negatively charged surface of silica nanoparticles. We hypothesize that the protein driven dissolution mechanism could be the primary reason for multiple metal ions release considering the binding affinity of FeNiCu ternary metal nanoparticles with a bacterial cell membrane or cytoplasmic protein functional groups. Figure 6b shows a schematic of protein driven oxidative dissolution of an FeNiCu ternary metal nanoparticle, where

proteins reduction and nanoparticle oxidation take place due to the electron transfer. The STEM-EDS results in Figure 5 support the hypothesis where the diffusion of metal cations in the organic corona is observed.

To confirm the binding affinity of FeNiCu ternary metal nanoparticles with bacterial cell membrane protein functional groups, additional *in vitro* binding affinity experiments were performed. To evaluate the binding affinity of metal nanoparticles with functional groups from the cellular proteins or lipopolysaccharides, the water-chloroform (polar-apolar) interface was utilized, where chemicals with an apolar ($-C_{17}H_{33}$) group having different polar functional groups ($-NH_2$ and $-COOH$) were dissolved in chloroform.[40] Oleylamine ($C_{17}H_{33}-NH_2$) and oleic acid ($C_{17}H_{33}-COOH$) were utilized as sources for the amine and carboxyl functional groups, respectively. Figure S6 in the Supporting Information shows the results from the *in vitro* binding affinity test of metal nanoparticles. As shown in Figure S6a FeNiCu ternary metal nanoparticles dispersed in water were separated at the top side due to the water-chloroform interface. Upon adding oleylamine and oleic acid in chloroform and a successive 10 min sonication, FeNiCu ternary metal nanoparticles were transferred into chloroform from water due to the binding with the functional groups. The results indicate that FeNiCu ternary metal nanoparticles can bind with amine ($-NH_2$) and carboxyl ($-COOH$) functional groups. Further, to evaluate the binding affinity of individual Cu, Ni, and Fe metal cations with amine and carboxyl functional groups, the *in vitro* affinity test with oleylamine and oleic acid was performed using unary Cu, unary Fe, and unary Ni nanoparticles. Figure S6b shows the binding affinities of unary Cu, unary Fe, and unary Ni metal nanoparticles with oleylamine. These results indicate that although unary Ni and unary Fe nanoparticles possess binding affinity with amine functional groups, unary Cu nanoparticles seem to possess stronger binding affinity. Figure S6c shows the binding affinities of unary Cu, unary Fe, and unary Ni metal nanoparticles with oleic acid. Unary Ni metal nanoparticles had the stronger binding affinity with the carboxyl group as compared with unary Cu and unary Fe metal nanoparticles. Briefly, the *in vitro* binding affinity test confirms the possible binding between cellular protein functional groups and FeNiCu ternary metal nanoparticles.

A bacterial cell membrane proteins selective binding affinity with multiple metal cations as a driving force is highlighted in Figure 6c. From the STEM-EDS results as observed in Figure 3 and Figure 5, it is evident that the Cu cations diffuse faster than nickel cations and iron cations from the core of FeNiCu ternary metal nanoparticles. Among different divalent metal cations Cu^{2+}, Ni^{2+}, and Fe^{2+} released from FeNiCu ternary nanoparticles, Cu^{2+} ions possess the highest affinity toward bacterial cell membrane metalloproteins.[46] The natural order of stability upon binding with divalent metal cations is defined by the Irving–Williams series.[47] Considering the structural flexibility of proteins, imperfect steric selection between different divalent metal cations takes place.[46] The binding affinity of divalent metal cations naturally appeared to follow the Irving–Williams series (Cu^{2+} > Ni^{2+} > Co^{2+} > Fe^{2+} > Mn^{2+} > Mg^{2+}).[46,47] Divalent copper (Cu^{2+}) tends to bind strongly with metalloproteins containing sulfur and nitrogen ligands, while monovalent copper (Cu^{1+}) is predominant in reducing bacterial cytosol.[46] As referred to in Figures 3–5, the enhanced release of copper ions could be possibly facilitated due to their highest binding affinity with cellular proteins. The *in vitro*

binding affinity test results, as referred to in Figure S6, confirmed the binding affinity of copper ions with amine ($-NH_2$) functional groups. The release of multiple metal cations from FeNiCu ternary metal nanoparticles upon interaction with bacterial cellular proteins seemed to follow the metal ions' release trend as per the Irving–William's series (Cu^{2+} > Ni^{2+} > Fe^{2+}).

In addition to the binding affinity dependent driving force, Figure 6d explains the possible reasons behind the faster outer diffusion of copper cations in comparison with nickel and iron metal cations. The nanoscale Kirkendall effect-atomic vacancy dependent model is well-known for understanding the competitive faster release of metal cations from the crystal lattice of nanoparticles.[48] Copper metal possesses specific attributes of being redox active and having a potential for promoting faster electron transfer as compared with iron.[49] The atomic radius for copper atoms is smaller than those for nickel and iron atoms (Cu^0 [128 pm] < Ni^0 [163 pm] < Fe^0 [194 pm]), which achieves the highest outward diffusion of copper atoms.[50] We hypothesize that the primary preferential binding affinity of bacterial cell membrane proteins with copper atoms in the FCC (face centered cubic) lattice of FeNiCu nanoparticles can primarily release the copper cations upon protein driven dissolution. Subsequently, the vacancies formed with the release of copper cations can possibly lose the intermetallic bonds within the FCC lattice of FeNiCu nanoparticles. By following the Irving–Williams series, successive release of Ni^{2+} ions can be promoted in the FeNiCu ternary nanoparticles. As observed in Figure 4, stronger intermetallic bonds between nickel atoms in unary Ni metal nanoparticles could result in decreased Ni^{2+} metal ions release as compared with FeNiCu ternary metal ions release. It was evident that the release of copper cations from multi-principal element FeNiCu metal nanoparticles was more favored than the release of nickel cations. Interestingly, Fe atoms have higher vacancy formation energy than Ni and Cu, indicating their lower diffusion in comparison to Ni and Cu. It is shown with atomistic calculations that the vacancy formation energy for Cu is less than that of Ni (1.27 versus 1.59 eV).[51] Experimentally, it is also shown that vacancy formation for Ni is less than that for Fe (1.78 versus 2 eV).[52] In our case, the diffusion of Cu atoms to the surface is expected to create vacancies that likely promote the diffusion of Ni atoms instead of Fe atoms. Overall, the present study will be insightful for developing antibacterial strategies where we can tune the composition of multi-principal element alloys and take advantage of compositional design for controlled release of multiple ions to deactivate bacteria. It will be interesting to perform similar *in situ* GLC-STEM elemental analysis studies of multielement nanoparticles against Gram-positive bacteria. Even though the *in situ* GLC-STEM approach provides nanoscale insights of bacteria and metal nanoparticles interactions, we would like to highlight that considering the delicacy and beam sensitivity of the specimens, this approach is mainly suitable for qualitative studies. For future quantitative and statistical analysis, ultrasmall fluorescence nanoprobes can be utilized for the detection of released metal ions in the bacterium cytoplasm.[53] To quantify the released multiple metal ions inside the bacterium cytoplasm, size exclusion chromatography coupled with the inductively coupled plasma-mass spectroscopy (SEC-ICP-MS) technique should be utilized in future studies.[54] In addition to the existing *in situ* GLC STEM approach, it will be interesting to study the interaction between
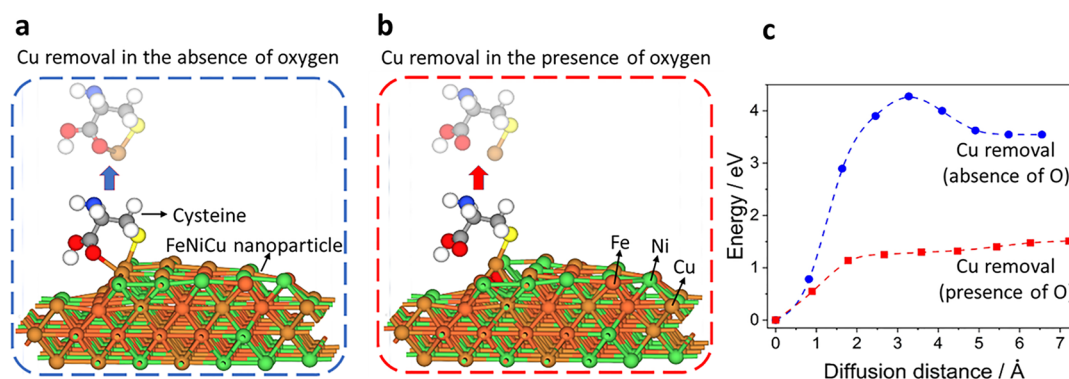
Figure 7. DFT calculation results of cysteine-Cu removal from the edge of the nanoparticle. (a) The corresponding removal in the absence of three oxygen atoms around the Cu edge atom. (b) The corresponding removal in the presence of three oxygen atoms around the Cu edge atom. (c) Graph illustrating the energetics obtained in the DFT calculations.

multielement nanoparticles and bacteria at two-dimensional (2D) and three-dimensional (3D) microscopic imaging levels using ultramicrotomy and laser ablation inductively coupled plasma mass spectroscopy (LA-ICP-MS) techniques, respectively.

Density functional theory (DFT) calculations are performed to understand better the molecular-level mechanism of the cysteine interaction with a multielement nanoparticle surface leading to the metal atoms removal. Experimentally it is observed that the protein interaction with the nanoparticle surface leads to Cu, Ni, and Fe atoms release. We have performed a series of *ab initio* calculations to shed light on a possible mechanistic interpretation behind such metal atoms removal. First, the most favorable atomic configuration of cysteine adsorption to Cu, Ni, and Fe atoms at the surface and edge of the multielement nanoparticle was calculated, followed by the nudge elastic band (NEB) calculations to reveal the energy barrier of the corresponding atoms release. Following the experimental results shown in Figure S1a and S1b, the multielement nanoparticle of composition Fe (34.24 at%), Ni (33.02 at%), and Cu (32.74 at%) was created (cf. Figure S7), and the DFT calculations are performed over such a nanoparticle surface as shown on the right in Figure S7. In order to create an experimentally similar multielement nanoparticle for DFT calculations, several multielement nanoparticle configurations varying elements' positions were considered. The ground-state energy of each such nanoparticle is very similar as long as the atomic percentage is preserved. Thus, one representative multielement nanoparticle was chosen for DFT calculations. Since the surface and subsurface composition around the nanoparticle are very similar, one representative slab was created by cleaving the first four layers of the nanoparticle.

Cysteine adsorption at the Cu, Ni, and Fe atoms over the flat surface and the edge of the cleaved nanoparticle was then calculated (cf. Figure S8). The observed trend is the same for the surface and edge adsorption. The binding energy of cysteine increases from Cu to Ni to Fe atom adsorption for both the surface and edge configurations. This indicates that the cysteine-Cu configuration is more prone to atom removal compared to the more stable cysteine-Fe structure. However, the binding energy only indicates the thermodynamic stability of a structure; kinetically, the vibration energy is the dominant factor of atom removal. Thus, we have performed a series of NEB calculations to evaluate the activation energy for cysteine-metal removal from the surface of a nanoparticle. Figure 7

shows the pathway (a and b) and the energetics (c, blue curve) of cysteine-Cu detachment from the edge of the nanoparticle. This process is energetically unfavorable by 3.6 eV and supported by a relatively high activation energy of 4.1 eV. A similar situation is observed for Ni and Fe atoms' removal from the edge of the nanoparticle by cysteine (cf. Figure S9). Specifically, Ni atom removal is even less favorable than Cu (4.4 eV) and is also supported by the higher activation energy of 5.2 eV. The cysteine-Fe removal is less favorable than Ni (5.6 eV), with the highest activation energy of 7 eV. Analyzing the thermodynamic and kinetic energetics of Cu, Ni, and Fe atoms' removal from the edge of the nanoparticle obtained in DFT calculations, it could be concluded that none of these processes proceed spontaneously, as observed in the experiment. Following the experimental results (cf. Figure 5), it could be observed that the surface of the nanoparticle may contain oxygen atoms in the form of adsorbates as well as metal oxides. This could change the stability of the cysteine-metal configuration since the neighboring atoms do not bind to the metal atom, but rather to oxygen atoms. To evaluate how the presence of the oxygen atoms influences Cu removal, we have added two and three oxygen atoms next to the Cu atom of the edge of the nanoparticle. Correspondingly, the thermodynamic and kinetic stabilities are calculated. Figure 7 shows the DFT calculation results of cysteine-Cu removal from the edge of the nanoparticle. The corresponding removal of the Cu edge atom by cysteine in the absence of three oxygen atoms is represented in Figure 7a. Figure 7b shows the corresponding removal of the Cu edge atom by cysteine in the presence of three oxygen atoms. By comparing the energetics of Cu removal (Figure 7c) in the absence of oxygen atoms, a significantly lower enthalpy (1.4 eV) could be observed with no activation energy. We have compared these calculations with the case of two surface oxygen atoms (cf. Figure S10). As can be observed comparing Figures 7 and S10, the addition of surface oxygen atoms decreases the stability of the cysteine-Cu configuration both thermodynamically and kinetically. This indicates that the energy to dissolve metal atoms exposed to oxidation and/or the presence of oxygen atoms at the surface of the nanoparticle catalyzes metal removal from the multielement nanoparticle, as observed in the experimental measurements. These findings are consistent with our hypothesis that the metal atom removal from the nanoparticle is a complex multistep mechanism where surface oxidation may play a crucial role. Additionally, the presence of the other elements, such as sulfur, nitrogen, etc., at the surface of the

nanoparticle may further reduce the energetics, leading to the favorable process of metal removal.

CONCLUSIONS

In summary, herein we propose the GLC-STEM approach to study the multiple metal ions release antibacterial mechanism of action. The use of the GLC approach can keep the electron beam sensitive organic soft matter in the hydrated state during the STEM data acquisition. The STEM-EDS results indicate that FeNiCu ternary nanoparticles were stable under the electron beam in the aqueous environment. As-synthesized control *E. coli* bacteria encapsulated in the GLC were stable under the electron beam by maintaining the cellular structural integrity, where STEM-EDS results confirm the presence of C, O, P, S, N, and Cl diagnostic ions within the bacterial cytoplasmic region. Upon interacting bacteria with FeNiCu ternary metal nanoparticles, the highest release of copper cations from FeNiCu metal nanoparticles was observed in the bacterium cytoplasmic region. The release of nickel cations from FeNiCu metal nanoparticles was lower than copper cations, while it was higher than the iron cations. The bacterium cytoplasmic components' leakage in the localized regions of nanoparticles was evaluated using the STEM-HAADF, STEM-LAADF, and STEM-EDS techniques. To understand the metal ions release dynamics from multi-principal element FeNiCu ternary metal nanoparticles, unary Fe, unary Ni, and unary Cu metal nanoparticles were studied for metal cations' release in the vicinity of bacteria using the *in situ* GLC STEM approach. The results showed that the release of copper ions from unary Cu metal nanoparticles was significant in bacterium cytoplasm, while there was almost no immediate release of nickel and iron metal cations from unary Ni and unary Fe metal nanoparticles, respectively. It was evident that release of copper cations from multi-principal element FeNiCu metal nanoparticles was more favored than release of nickel cations. The highest release and outward diffusion of copper cations from FeNiCu ternary metal nanoparticles was observed in the organic protein corona around a nanoparticle, signifying the importance of interaction with functional groups present in the bacterial cell membrane proteins. The binding affinity of bacterial cell membrane protein functional groups with Cu, Ni, and Fe divalent cations is possibly the driving force behind the selective metal cations' release from the multi-principal element nanoparticles following the Irving−Williams series ($Cu^{2+} > Ni^{2+} > Fe^{2+}$). The DFT calculations confirmed that the dissolution of FeNiCu nanoparticles by the protein functional group (cysteine amino acid) energetically favors the removal of Cu atoms followed by Ni atoms, while the removal of Fe atoms was favored the least. The computational results support the experimental data, indicating that the energy to dissolve metal atoms exposed to oxidation and/or the presence of oxygen atoms at the surface of the nanoparticle catalyzes metal removal from the multielement nanoparticle.

EXPERIMENTAL METHODS

Fabrication of Graphene Coated TEM Grids. Graphene coated TEM grids were prepared by using a protocol described by Hauwiller et al.[55] Briefly, a monolayer of commercially CVD grown graphene coated copper foil (Grolltex, monolayer graphene on copper foil 6′′ × 6′′) was used as a graphene source. A 1 cm × 1 cm piece of graphene coated copper foil was cut using a surgical grade scalpel. The wrinkles from the graphene coated copper foil were removed using a couple of glass slides and nonwoven wipers (Texwipe, TX629). Quantifoil micromachined holey carbon coated 200 mesh gold grids (SPI supplies, 4220G-XA) were placed on the flattened graphene coated copper foil, assuring the carbon side of the grids remains in contact with the graphene layer. Successively, 15 μL of isopropyl alcohol was dropped on the graphene coated copper foil to improve the van der Waals interactions between the graphene and the holey carbon layer of the TEM grids. Upon drying after 2 h, the graphene coated copper foil along with the TEM grids were placed in a sodium persulfate solution (Millipore Sigma, 216232) as a copper etchant for 12 h. After copper foil etching, the floating gold TEM grids were transferred into HPLC grade water (Millipore Sigma, 7732-18-5) using two glass slides. Finally, after repeating the rinsing process 3 times, the graphene coated TEM grids were air-dried.

Synthesis of Metal Nanoparticles Using Aerosol Spray Pyrolysis. Ternary FeNiCu, unary Fe, unary Ni, and unary Cu metal nanoparticles were synthesized using the aerosol spray pyrolysis method.[33] Iron nitrate nonahydrate [$Fe(NO_3)_3 \cdot 9H_2O$, ≥99% pure], nickel nitrate hexahydrate [$Ni(NO_3)_2 \cdot 6H_2O$, ≥99% pure], and copper nitrate trihydrate [$Cu(NO_3)_2 \cdot 3H_2O$, ≥99% pure] were purchased from Sigma-Aldrich as aprecursors for producing Fe, Ni and Cu unary metal nanoparticles. For synthesizing FeNiCu ternary metal nanoparticles, metal salt precursors were used in equimolar ratio (0.02 M) using deionized water as a solvent. Briefly, the metal salt precursor solution was nebulized, producing small aerosol droplets using 10% H_2/90% Ar mixture gas at 30 psi. The produced aerosol droplets were then flowed through a 1100 °C heating zone at a 3 L/min flow rate to produce FeNiCu ternary metal nanoparticles. For unary metal nanoparticles, the same synthesis protocol was utilized.

***Escherichia coli* Bacteria Culture.** The *E. coli* K12 g-negative bacteria strain (ATCC29425) was utilized as bacteria source. For preparing bacteria cultures, Luria Broth (Miller's LB Broth_L24040-500.0) and molecular grade water (248700) were obtained from Research Products International (RPI), USA. The bacteria culture was prepared by inoculating *E. coli* in sterilized LB broth medium. Successively, the medium was incubated for 6 h at 37 °C under shaking to achieve 10^4 CFU/mL concentration. The cultured *E. coli* bacteria were centrifuged at 4500 rpm for 15 min, and the supernatant media was discarded. The *E. coli* bacteria pallet was dispersed in molecular grade water for rinsing, and immediately the centrifugation step was implemented. The rinsing process was repeated a couple of times. Final rinsed cultured *E. coli* bacteria were used for *in situ* GLC STEM studies.

Graphene Liquid Cell Encapsulation of Reaction Solution. Two graphene coated TEM grids were used to prepare final encapsulation to prepare reaction solution. Inverted TEM tweezers were used for preparing the GLCs. For preparing the reaction solution, the cultured *E. coli* bacteria (100 CFU/mL concentration) and metal nanoparticles (10 μg/mL concentration) were mixed in ultrapure water as a medium and were allowed to interact under shaking for 3 min. 0.3 μL of prepared solution was encapsulated between two graphene coated TEM grids to prepare GLC.

STEM Characterization. An aberration corrected JEOL ARM200CF transmission electron microscope (200 kV) equipped with a cold field emission gun was used for performing *in situ* GLC STEM studies. Upon encapsulation, GLC grids were loaded on the single tilt TEM holder. The emission current was reduced up to 10 μA. An electron beam convergence angle of 22 mrad at an 8c probe size was used for performing STEM-HAADF and STEM-LAADF imaging with an Orius CCD camera at 512 × 512 pixels scanning resolution. STEM-EDS analysis was performed using the Oxford EDS system at 5c probe size synchronized with a drift corrector and operated at a 5 μS pixel dwell time.

COMPUTATIONAL METHODS

Density Functional Theory (DFT) Calculations. The Vienna Ab Initio Simulations Package (VASP) code was used to perform the DFT calculations employing the generalized-gradient approximation (GGA)[56] and the PBE (Perdew, Burke, and Ernzerhof)[57] functional to account for the exchange-correlation effects. For systems with an

odd number of electrons non-spin-polarized calculations and for systems with even numbers of electrons spin polarized calculations were performed. Metal atom migration paths and barriers were determined using the linear nudged elastic band (NEB) method as realized in the VASP code. A cutoff energy of 450 eV was used for all calculations. The further increase of cutoff energy lead to minor changes of ground-state energy; however, it increased the calculation time significantly. Thus, 450 eV, as the optimal value considering the change of the ground-state energy and calculation time, was used. All structural optimizations were carried out until the forces, acting on atoms, were below 0.01 eV/Å. The criterion for energy change was set to 0.1 eV. All nanoparticle and slabs were created using the Atomistic Tool Kit (ATK).[58]

ASSOCIATED CONTENT

Ⓢ Supporting Information

The Supporting Information is available free of charge at https://pubs.acs.org/doi/10.1021/acsnano.2c12799.

> **Figure S1** representing the STEM-HAADF and STEM-EDS analysis of FeNiCu ternary metal nanoparticles, **Figure S2** indicating the additional regions of *in situ* GLC STEM-EDS analysis of control *E. coli* bacteria, **Figure S3** representing the TEM and STEM micrographs of FeNiCu ternary metal nanoparticles in the vicinity of bacteria in the aqueous environment upon encapsulating in a GLC, **Figure S4** indicating the additional regions of *in situ* GLC STEM-EDS analysis of interaction of FeNiCu multielement nanoparticles with *E. coli* bacteria, **Figure S5** representing the additional regions of *in situ* GLC STEM-EDS analysis of interaction of respective unary-Cu, unary-Ni, and, unary-Fe nanoparticles with *E. coli* bacteria, **Figure S6** representing the results from binding affinity qualitative tests of metal nanoparticles with bacterial cell membrane functional groups, **Figure S7** showing the DFT model of formation of the nanoparticle structure, **Figure S8** representing the illustration of the atomic structure of cysteine interaction with surface and edge Cu, Ni and Fe atoms, **Figure S9** representing the path and the energetics of the edge Ni (a) and Fe (b) atoms' removal by cysteine, and **Figure S10** representing the path and the energetics of the edge Cu atom removal by cysteine in the presence of two surface oxygen atoms near the Cu atom. (PDF)

AUTHOR INFORMATION

Corresponding Authors

Tolou Shokuhfar − *Department of Biomedical Engineering, University of Illinois Chicago, Chicago, Illinois 60607, United States*

Reza Shahbazian-Yassar − *Department of Mechanical and Industrial Engineering, University of Illinois Chicago, Chicago, Illinois 60607, United States;* ⓘ orcid.org/0000-0002-7744-4780

Authors

Abhijit H. Phakatkar − *Department of Biomedical Engineering, University of Illinois Chicago, Chicago, Illinois 60607, United States*

Vitaliy Yurkiv − *Department of Aerospace and Mechanical Engineering, University of Arizona, Tucson, Arizona 85721, United States*

Pankaj Ghildiyal − *Department of Chemical and Environmental Engineering, University of California,*

Riverside, California 92521, United States; Department of Chemistry and Biochemistry, University of Maryland, College Park, Maryland 20742, United States; ⓘ orcid.org/0000-0002-4422-3068

Yujie Wang − *Department of Chemical and Environmental Engineering, University of California, Riverside, California 92521, United States*

Azadeh Amiri − *Department of Mechanical and Industrial Engineering, University of Illinois Chicago, Chicago, Illinois 60607, United States*

Lioudmila V. Sorokina − *Department of Civil, Materials, and Environmental Engineering, University of Illinois Chicago, Chicago, Illinois 60607, United States*

Michael R. Zachariah − *Department of Chemical and Environmental Engineering, University of California, Riverside, California 92521, United States;* ⓘ orcid.org/0000-0002-4115-3324

Complete contact information is available at:
https://pubs.acs.org/10.1021/acsnano.2c12799

Author Contributions

A.H.P. performed the *in situ* GLC STEM bacteria−nanoparticles experiment and wrote the manuscript. P.G. and Y.W. synthesized metal nanoparticles under the guidance of M.R.Z. V.Y. performed the computational DFT analysis and wrote the computational results section in the manuscript. A.A. and L.V.S. contributed to evaluating the discussion section evaluating the metal ions' release antibacterial mechanism from multi-principal element nanoparticles. R.S.Y. and T.S. conceptualized and supervised the project. All authors proofread, commented on, and approved the final manuscript for submission.

Notes

The authors declare no competing financial interest.

ABBREVIATIONS

E. coli, *Escherichia coli*; GLC, graphene liquid cell; STEM, scanning transmission electron microscopy; AMR, antimicrobial resistance; ROS, reactive oxygen species; DNA, DNA; mRNA, messenger ribonucleic acid; ATP, adenosine triphosphate; ZnO, zinc oxide; CuO, copper oxide; TEM, transmission electron microscopy; EDS, energy dispersive X-ray spectroscopy; HAADF, high angle annular dark field; LAADF, low angle annular dark field; DFT, density functional theory; NEB, nudged elastic band; VASP, Vienna Ab Initio Simulations Package; ATK, Atomistic Tool Kit

REFERENCES

(1) Mahase, E. Changes in behaviour last year led to fall in antibiotic resistant infections. *British Medical Journal* **2021**, *375*, n2853.

(2) Ansari, M.; Kuche, K.; Ghadi, R.; Chaudhari, D.; Ansari, F. A.; Khan, R.; Vyawahare, A.; Jain, S. Nanoparticles as a Future Alternative Against Multiple Drug Resistance. *Emerging Modalities in Mitigation of Antimicrobial Resistance*; Springer, 2022; pp 423−439.

(3) Malka, E.; Perelshtein, I.; Lipovsky, A.; Shalom, Y.; Naparstek, L.; Perkas, N.; Patick, T.; Lubart, R.; Nitzan, Y.; Banin, E. Eradication of multi-drug resistant bacteria by a novel Zn-doped CuO nanocomposite. *Small* **2013**, *9* (23), 4069−4076.

(4) Slavin, Y. N.; Asnis, J.; Häfeli, U. O.; Bach, H. Metal nanoparticles: understanding the mechanisms behind antibacterial activity. *J. Nanobiotechnol.* **2017**, *15* (1), 1−20.

(5) Feng, Q. L.; Wu, J.; Chen, G. Q.; Cui, F.; Kim, T.; Kim, J. A mechanistic study of the antibacterial effect of silver ions on Escherichia coli and Staphylococcus aureus. *J. Biomed. Mater. Res.* **2000**, *52* (4), 662−668.

(6) Graves, J. L., Jr; Tajkarimi, M.; Cunningham, Q.; Campbell, A.; Nonga, H.; Harrison, S. H.; Barrick, J. E. Rapid evolution of silver nanoparticle resistance in Escherichia coli. *Frontiers in genetics* **2015**, *6*, 42.

(7) Gupta, A.; Silver, S. Molecular genetics: silver as a biocide: will resistance become a problem? *Nature biotechnology* **1998**, *16* (10), 888−888.

(8) Kaweeteerawat, C.; Na Ubol, P.; Sangmuang, S.; Aueviriyavit, S.; Maniratanachote, R. Mechanisms of antibiotic resistance in bacteria mediated by silver nanoparticles. *Journal of Toxicology and Environmental Health, Part A* **2017**, *80* (23−24), 1276−1289.

(9) Ouyang, K.; Mortimer, M.; Holden, P. A.; Cai, P.; Wu, Y.; Gao, C.; Huang, Q. Towards a better understanding of Pseudomonas putida biofilm formation in the presence of ZnO nanoparticles (NPs): Role of NP concentration. *Environ. Int.* **2020**, *137*, 105485.

(10) Bakina, O.; Glazkova, E.; Svarovskaya, N.; Rodkevich, N.; Lerner, M. ≪Janus≫-like Cu-Fe bimetallic nanoparticles with high antibacterial activity. *Materials letters* **2019**, *242*, 187−190.

(11) Benetti, G.; Cavaliere, E.; Brescia, R.; Salassi, S.; Ferrando, R.; Vantomme, A.; Pallecchi, L.; Pollini, S.; Boncompagni, S.; Fortuni, B. Tailored Ag-Cu-Mg multielemental nanoparticles for wide-spectrum antibacterial coating. *Nanoscale* **2019**, *11* (4), 1626−1635.

(12) Zhang, M.; Chen, W.; Choi, W.; Yu, J.; Deng, Y.; Xie, X.; Lin, Z. Ternary Biocidal-Photocatalytic-Upconverting Nanocomposites for Enhanced Antibacterial Activity. *ACS Sustainable Chem. Eng.* **2022**, *10* (14), 4741−4749.

(13) Arora, N.; Thangavelu, K.; Karanikolos, G. N. Bimetallic nanoparticles for antimicrobial applications. *Frontiers in Chemistry* **2020**, *8*, 412.

(14) Wang, L.; Hu, C.; Shao, L. The antimicrobial activity of nanoparticles: present situation and prospects for the future. *International journal of nanomedicine* **2017**, *12*, 1227.

(15) Kloepfer, J.; Mielke, R.; Nadeau, J. Uptake of CdSe and CdSe/ZnS quantum dots into bacteria via purine-dependent mechanisms. *Applied and environmental microbiology* **2005**, *71* (5), 2548−2557.

(16) Linklater, D. P.; Baulin, V. A.; Le Guével, X.; Fleury, J. B.; Hanssen, E.; Nguyen, T. H. P.; Juodkazis, S.; Bryant, G.; Crawford, R. J.; Stoodley, P. Antibacterial action of nanoparticles by lethal stretching of bacterial cell membranes. *Adv. Mater.* **2020**, *32* (52), 2005679.

(17) Sousa de Almeida, M.; Susnik, E.; Drasler, B.; Taladriz-Blanco, P.; Petri-Fink, A.; Rothen-Rutishauser, B. Understanding nanoparticle endocytosis to improve targeting strategies in nanomedicine. *Chem. Soc. Rev.* **2021**, *50* (9), 5397−5434.

(18) Gao, F.; Shao, T.; Yu, Y.; Xiong, Y.; Yang, L. Surface-bound reactive oxygen species generating nanozymes for selective antibacterial action. *Nat. Commun.* **2021**, *12*, 745.

(19) Cizmar, P.; Yuana, Y. Detection and characterization of extracellular vesicles by transmission and cryo-transmission electron microscopy. *Extracellular Vesicles*; Springer, 2017; pp 221−232.

(20) Kennedy, E.; Nelson, E. M.; Tanaka, T.; Damiano, J.; Timp, G. Live bacterial physiology visualized with 5 nm resolution using scanning transmission electron microscopy. *ACS Nano* **2016**, *10* (2), 2669−2677.

(21) Kuo, J.-C.; Tan, S.-H.; Hsiao, Y.-C.; Mutalik, C.; Chen, H.-M.; Yougbaré, S.; Kuo, T.-R. Unveiling the antibacterial mechanism of gold nanoclusters via in situ transmission electron microscopy. *ACS Sustainable Chem. Eng.* **2022**, *10* (1), 464−471.

(22) Narayanan, S.; Shahbazian-Yassar, R.; Shokuhfar, T. In situ visualization of ferritin biomineralization via graphene liquid cell-transmission electron microscopy. *ACS Biomaterials Science & Engineering* **2020**, *6* (5), 3208−3216.

(23) Wang, C.; Qiao, Q.; Shokuhfar, T.; Klie, R. F. High-resolution electron microscopy and spectroscopy of ferritin in biocompatible graphene liquid cells and graphene sandwiches. *Adv. Mater.* **2014**, *26* (21), 3410−3414.

(24) Firlar, E.; Ouy, M.; Covnot, L.; Xing, Y.; Lee, D.; Chan, A.; He, Y.; Song, B.; Afelik, S.; Wang, Y. In situ graphene liquid cell-transmission electron microscopy study of insulin secretion in pancreatic islet cells. *Int. J. Nanomed.* **2019**, *14*, 371.

(25) Ghodsi, S. M.; Megaridis, C. M.; Shahbazian-Yassar, R.; Shokuhfar, T. Advances in Graphene-Based Liquid Cell Electron Microscopy: Working Principles, Opportunities, and Challenges. *Small Methods* **2019**, *3* (5), 1900026.

(26) Firlar, E.; Ouy, M.; Bogdanowicz, A.; Covnot, L.; Song, B.; Nadkarni, Y.; Shahbazian-Yassar, R.; Shokuhfar, T. Investigation of the magnetosome biomineralization in magnetotactic bacteria using graphene liquid cell-transmission electron microscopy. *Nanoscale* **2019**, *11* (2), 698−705.

(27) Mohanty, N.; Fahrenholtz, M.; Nagaraja, A.; Boyle, D.; Berry, V. Impermeable graphenic encasement of bacteria. *Nano Lett.* **2011**, *11* (3), 1270−1275.

(28) Wang, C.; Shokuhfar, T.; Klie, R. F. Precise in situ modulation of local liquid chemistry via electron irradiation in nanoreactors based on graphene liquid cells. *Adv. Mater.* **2016**, *28* (35), 7716−7722.

(29) Cho, H.; Jones, M. R.; Nguyen, S. C.; Hauwiller, M. R.; Zettl, A.; Alivisatos, A. P. The use of graphene and its derivatives for liquid-phase transmission electron microscopy of radiation-sensitive specimens. *Nano Lett.* **2017**, *17* (1), 414−420.

(30) Vincent, M.; Duval, R. E.; Hartemann, P.; Engels-Deutsch, M. Contact killing and antimicrobial properties of copper. *Journal of applied microbiology* **2018**, *124* (5), 1032−1046.

(31) Gudkov, S. V.; Burmistrov, D. E.; Serov, D. A.; Rebezov, M. B.; Semenova, A. A.; Lisitsyn, A. B. Do iron oxide nanoparticles have significant antibacterial properties? *Antibiotics* **2021**, *10* (7), 884.

(32) Ahghari, M. R.; Soltaninejad, V.; Maleki, A. Synthesis of nickel nanoparticles by a green and convenient method as a magnetic mirror with antibacterial activities. *Sci. Rep.* **2020**, *10* (1), 1−10.

(33) Yang, Y.; Song, B.; Ke, X.; Xu, F.; Bozhilov, K. N.; Hu, L.; Shahbazian-Yassar, R.; Zachariah, M. R. Aerosol synthesis of high entropy alloy nanoparticles. *Langmuir* **2020**, *36* (8), 1985−1992.

(34) Phakatkar, A. H.; Firlar, E.; Alzate, L.; Song, B.; Narayanan, S.; Rojaee, R.; Foroozan, T.; Deivanayagam, R.; Banner, D. J.; Shahbazian-Yassar, R. TEM studies on antibacterial mechanisms of black phosphorous nanosheets. *Int. J. Nanomed.* **2020**, *15*, 3071.

(35) Liu, J. L.; Luo, Z.; Bashir, S. A progressive approach on inactivation of bacteria using silver-titania nanoparticles. *Biomaterials science* **2013**, *1* (2), 194−201.

(36) Mesibov, R.; Adler, J. Chemotaxis toward amino acids in Escherichia coli. *J. Bacteriol.* **1972**, *112* (1), 315−326.

(37) Fagerbakke, K. M.; Heldal, M.; Norland, S. Content of carbon, nitrogen, oxygen, sulfur and phosphorus in native aquatic and cultured bacteria. *Aquatic Microbial Ecology* **1996**, *10* (1), 15−27.

(38) Fulaz, S.; Vitale, S.; Quinn, L.; Casey, E. Nanoparticle-biofilm interactions: the role of the EPS matrix. *Trends in microbiology* **2019**, *27* (11), 915−926.

(39) Ribeiro, A.; Gemini-Piperni, S.; Travassos, R.; Lemgruber, L.; Silva, R. C.; Rossi, A.; Farina, M.; Anselme, K.; Shokuhfar, T.; Shahbazian-Yassar, R. Trojan-like internalization of anatase titanium dioxide nanoparticles by human osteoblast cells. *Sci. Rep.* **2016**, *6* (1), 1−11.

(40) Peng, B.; Zhang, X.; Aarts, D. G.; Dullens, R. Superparamagnetic nickel colloidal nanocrystal clusters with antibacterial

activity and bacteria binding ability. *Nature Nanotechnol.* **2018**, *13* (6), 478−482.

(41) Lynch, I.; Cedervall, T.; Lundqvist, M.; Cabaleiro-Lago, C.; Linse, S.; Dawson, K. A. The nanoparticle-protein complex as a biological entity; a complex fluids and surface science challenge for the 21st century. *Advances in colloid and interface science* **2007**, *134*, 167−174.

(42) Sahu, D. K.; Sarkar, P.; Singha, D.; Sahu, K. Protein-activated transformation of silver nanoparticles into blue and red-emitting nanoclusters. *RSC Adv.* **2019**, *9* (67), 39405−39409.

(43) Fukushima, T.; Gupta, S.; Rad, B.; Cornejo, J. A.; Petzold, C. J.; Chan, L. J. G.; Mizrahi, R. A.; Ralston, C. Y.; Ajo-Franklin, C. M. The molecular basis for binding of an electron transfer protein to a metal oxide surface. *J. Am. Chem. Soc.* **2017**, *139* (36), 12647−12654.

(44) Martinolich, A. J.; Park, G.; Nakamoto, M. Y.; Gate, R. E.; Wheeler, K. E. Structural and functional effects of Cu metalloprotein-driven silver nanoparticle dissolution. *Environ. Sci. Technol.* **2012**, *46* (11), 6355−6362.

(45) Ali, M. S.; Uttinger, M. J.; Romeis, S.; Schmidt, J.; Peukert, W. Effect of protein adsorption on the dissolution kinetics of silica nanoparticles. *Colloids Surf., B* **2022**, *214*, 112466.

(46) Waldron, K. J.; Robinson, N. J. How do bacterial cells ensure that metalloproteins get the correct metal? *Nature Reviews Microbiology* **2009**, *7* (1), 25−35.

(47) Irving, H.; Williams, R. Order of stability of metal complexes. *Nature* **1948**, *162* (4123), 746−747.

(48) Railsback, J. G.; Johnston-Peck, A. C.; Wang, J.; Tracy, J. B. Size-dependent nanoscale Kirkendall effect during the oxidation of nickel nanoparticles. *ACS Nano* **2010**, *4* (4), 1913−1920.

(49) Bhagi-Damodaran, A.; Michael, M. A.; Zhu, Q.; Reed, J.; Sandoval, B. A.; Mirts, E. N.; Chakraborty, S.; Moënne-Loccoz, P.; Zhang, Y.; Lu, Y. Why copper is preferred over iron for oxygen activation and reduction in haem-copper oxidases. *Nature Chem.* **2017**, *9* (3), 257−263.

(50) Song, B.; Yang, Y.; Rabbani, M.; Yang, T. T.; He, K.; Hu, X.; Yuan, Y.; Ghildiyal, P.; Dravid, V. P.; Zachariah, M. R. In situ oxidation studies of high-entropy alloy nanoparticles. *ACS Nano* **2020**, *14* (11), 15131−15143.

(51) Nemirovich-Danchenko, L. Y.; Lipnitskĭ, A.; Kul'kova, S. Vacancies and their complexes in FCC metals. *Phys. Solid State* **2007**, *49* (6), 1079−1085.

(52) Nandi, P. K.; Valsakumar, M.; Chandra, S.; Sahu, H.; Sundar, C. Efficacy of surface error corrections to density functional theory calculations of vacancy formation energy in transition metals. *J. Phys.: Condens. Matter* **2010**, *22* (34), 345501.

(53) Kateshiya, M. R.; Desai, M. L.; Malek, N. I.; Kailasa, S. K. Advances in Ultra-small Fluorescence Nanoprobes for Detection of Metal Ions, Drugs, Pesticides and Biomarkers. *J. Fluoresc.* **2022**, 1−24.

(54) Dong, L.-J.; Lai, Y.-J.; Yu, S.-J.; Liu, J.-F. Speciation analysis of the uptake and biodistribution of nanoparticulate and ionic silver in Escherichia coli. *Analytical chemistry* **2019**, *91* (19), 12525−12530.

(55) Hauwiller, M. R.; Ondry, J. C.; Alivisatos, A. P. Using graphene liquid cell transmission electron microscopy to study in situ nanocrystal etching. *JoVE (Journal of Visualized Experiments)* **2018**, No. 135, No. e57665.

(56) Perdew, J. P.; Chevary, J.; Vosko, S.; Jackson, K. A.; Pederson, M. R.; Singh, D.; Fiolhais, C. Erratum: Atoms, molecules, solids, and surfaces: Applications of the generalized gradient approximation for exchange and correlation. *Phys. Rev. B* **1993**, *48* (7), 4978.

(57) Perdew, J. P.; Burke, K.; Ernzerhof, M. Generalized gradient approximation made simple. *Physical review letters* **1996**, *77* (18), 3865.

(58) Smidstrup, S.; Markussen, T.; Vancraeyveld, P.; Wellendorff, J.; Schneider, J.; Gunst, T.; Verstichel, B.; Stradi, D.; Khomyakov, P. T.; Vej-Hansen, U. G. QuantumATK: An integrated platform of electronic and atomic-scale modelling tools. *J. Phys.: Condens. Matter* **2020**, *32*, 015901.